

Journal of
Applied Remote Sensing

**Airborne lidar detection and
characterization of internal waves in a
shallow fjord**

James H. Churnside
Richard D. Marchbanks
Jennifer H. Lee
Joseph A. Shaw
Alan Weidemann
Percy L. Donaghay

Airborne lidar detection and characterization of internal waves in a shallow fjord

James H. Churnside,^a Richard D. Marchbanks,^b Jennifer H. Lee,^a
Joseph A. Shaw,^c Alan Weidemann,^d and Percy L. Donaghay^e

^aNOAA Earth System Research Laboratory, 325 Broadway, Boulder, Colorado 80305-3337
james.h.churnside@noaa.gov

^bUniversity of Colorado and NOAA Earth System Research Laboratory, Cooperative
Institute for Research in the Environmental Sciences, 325 Broadway, Boulder, Colorado
80305-3337

^cMontana State University, Optical Technology Center and Electrical & Computer Engineering
Department, Bozeman, Montana 59717

^dNaval Research Laboratory, Stennis Space Center, Mississippi, 39529

^eUniversity of Rhode Island, Graduate School of Oceanography, Narragansett,
Rhode Island 02874

Abstract. A dual-polarization lidar and photography are used to sense internal waves in West Sound, Orcas Island, Washington, from a small aircraft. The airborne lidar detected a thin plankton layer at the bottom of the upper layer of the water, and this signal provides the depth of the upper layer, amplitude of the internal waves, and the propagation speed. The lidar is most effective when the polarization filter on the receiver is orthogonal to the transmitted light, but this does not depend significantly on whether the transmitted light is linearly or circularly polarized. The depolarization is greater with circular polarization, and our results are consistent with a single parameter Mueller scattering matrix. Photographs of the surface manifestation of the internal waves clearly show the propagation direction and width of the phase fronts of the internal waves, even though the contrast is low (2%). Combined with the lidar profile, the total energy of the internal wave packet was estimated to be 9 MJ. © 2012 Society of Photo-Optical Instrumentation Engineers (SPIE). [DOI: [10.1117/1.JRS.6.063611](https://doi.org/10.1117/1.JRS.6.063611)]

Keywords: ocean optics; lidar; internal waves; plankton; thin layers.

Paper 12162P received May 31, 2012; revised manuscript received Oct. 22, 2012; accepted for publication Nov. 6, 2012; published online Dec. 5, 2012.

1 Introduction

Waves on the surface of the ocean are a common sight, but internal waves are less familiar. Internal waves propagate along density gradients within the ocean much like surface waves propagate along the air/water density interface. In the ocean, solar heating at the surface and/or fresh water input from terrestrial runoff or melting ice create a layer of water with lower density at the surface. This layer is typically mixed with the water below by the action of surface waves and turbulence, but this is only effective to some finite depth that depends on the strength of the wind. This tends to create a layer of less dense water on top of the more dense water below. The boundary, known as the pycnocline, is the region of large density gradients on which internal waves propagate. Of course, the real ocean is more complex, and multiple layers may form from episodic heating and mixing events.

Internal waves are an important process in mixing in the ocean.¹⁻³ One of the most common processes for the generation in internal waves is the flow of tidal currents over bottom topography,⁴ especially at the edge of the continental shelf. These waves can propagate over long distances, carrying this tidal energy with them. This energy is eventually released and dissipated where the waves break.⁵

The surface signatures from internal waves have been observed in microwave-radar data.^{6–9} The primary mechanism is the modulation of surface roughness, which is the source of the radar signal, by the surface currents produced by the waves.^{8,10,11} Where surface currents are diverging, the roughness is decreased, and the radar return is reduced. Where currents are converging, the roughness is increased, and the radar return is increased.

For these waves to be apparent in a lidar signal, there has to be some tracer, such as a layer of phytoplankton to scatter the light. Fortunately, such a layer often exists near the pycnocline. In the simplified two-layer model of the ocean, one can imagine that the nutrients in the upper layer would be consumed rapidly since there is plenty of sunlight for photosynthesis. The lower layer represents a large reservoir of nutrients, but there is little sunlight. The result is a narrow zone near the pycnocline that will support phytoplankton growth.¹² This is oversimplified, and other processes that contribute to thin-layer formation include stretching of a plankton patch into a layer by current shear and sinking of plankton cells until they reach the depth where their density matches that of the surrounding water.^{13–15} Regardless of the mechanism, thin plankton layers associated with the pycnocline have been observed,^{13,14} and the detection of scattering layers, including thin plankton layers, by airborne lidar is well documented.^{12,16–19} We have demonstrated that these thin layers can be associated with upwelling events and with fresh water influx.¹⁸

Acoustic measurements have shown that these thin layers move up and down under the influence of internal waves,¹⁹ and internal waves also have been observed in airborne lidar data.^{18,20} However, neither of these lidar observations had coincident in-water measurements for comparison. This paper reports on lidar and photographic measurements of several internal waves in West Sound on Orcas Island in Washington state, and the comparison with *in situ* measurements of water stratification and optical properties. The primary objective was to determine whether or not the energy of an internal-wave packet can be obtained from remote sensing data collected by lidar and aerial photography. A secondary objective was to determine if quantitative information could also be obtained about turbulence within the plankton layers.

In previous studies, it was observed that the lidar signal from a plankton layer has higher contrast (i.e., stands out more clearly against the lidar signal from the surrounding water) when the laser transmitter is linearly polarized and the receiver is filtered to collect scattered light in the orthogonal polarization.^{17,18,20} The reason is that plankton are much larger than the 532-nm wavelength that is generally used for oceanographic lidar and have enough irregularly shaped structures to depolarize backscattered light through multiple scattering within each cell or colony. Previous work has suggested that circularly polarized light will provide better contrast for large underwater targets,^{21–23} but does not have a corresponding advantage for a collection of small particles.^{24–27} A third objective of this work was to compare the contrast for linear and circular polarizations.

2 Measurements

East Sound on Orcas Island in Washington state has been the site of a number of studies on thin layer formation and evolution.^{12,14,28–30} This history of plankton layer formation led us to return to East Sound in September 2011 with the airborne lidar. No significant evidence of plankton layers was found in the lidar data from flights over East Sound in September of 2011, so we moved to West Sound to make the measurements. Only data from West Sound are considered in this analysis. While both East Sound and West Sound are shallow fjords that are protected by other islands to the south (Fig. 1), West Sound is smaller and more open to internal waves that can be generated by the strong tidal flows through the channel outside the sound.

The NOAA Fish Lidar,^{31–33} developed in the Earth System Research Laboratory over a number of years, was installed in the back of a four-seat Cessna-177 aircraft with the rear seats removed (Fig. 2). Two flights were made each day of the deployment at a flight altitude of about 300 m and a speed of about 40 m s⁻¹. The lidar transmitted 100 mJ of green (532 nm) light in a 12-ns pulse at a rate of 10 pulses per second. It was pointed 12 deg off nadir to minimize the specular reflection from the sea surface. The laser beam divergence was set so that the diameter of the laser spot on the surface was 5 m, which is large enough that the power density at the

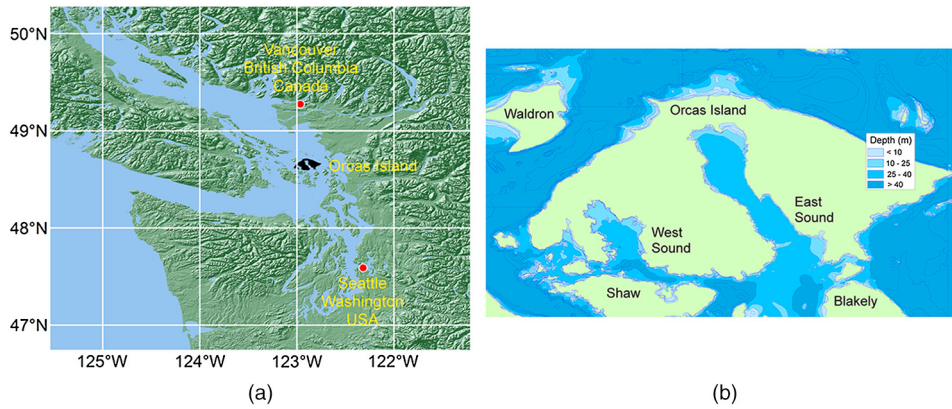


Fig. 1 Map of Orcas Island and surroundings. (a) Location of Orcas Island (black) in the north-western United States between Vancouver, British Columbia, and Seattle, Washington; (b) Orcas Island and surrounding islands, showing East Sound, which is about 10 km long, and West Sound, which is about half of that. The large bay on the east side of West Sound is White Beach Bay.

surface is safe for humans and marine mammals.³⁴ The scattered light from the water column was collected by two telescopes whose fields of view were matched to the laser beam divergence. Each telescope was equipped [as shown in Fig. 2(a)] with a polarizing filter, a field-of-view aperture, and an interference filter to reduce background light. The light collected by each telescope was detected by a photomultiplier tube, logarithmically amplified to increase the dynamic range, and digitized at a rate of 10^9 samples per second. Between the morning flight and the afternoon flight on September 16, we changed the polarization characteristics of the lidar. In the morning, the transmitter was linearly polarized, and the two telescopes were filtered to receive light co-polarized with the transmitter and cross-polarized to it. In the afternoon, the transmitter was changed to right-hand circular polarization, and the receiver telescopes were filtered to receive co- and cross-circularly polarized light.

Identification of internal waves in the lidar data was by visual inspection. The raw cross-polarized lidar data was used for this because of the improved contrast, which facilitated layer detection; the layers were much less visible in the co-polarized return. Data segments with visible wave structure were processed further to correct for the exponential attenuation and to subtract the background scattering to enhance the visibility of the layers. The depth

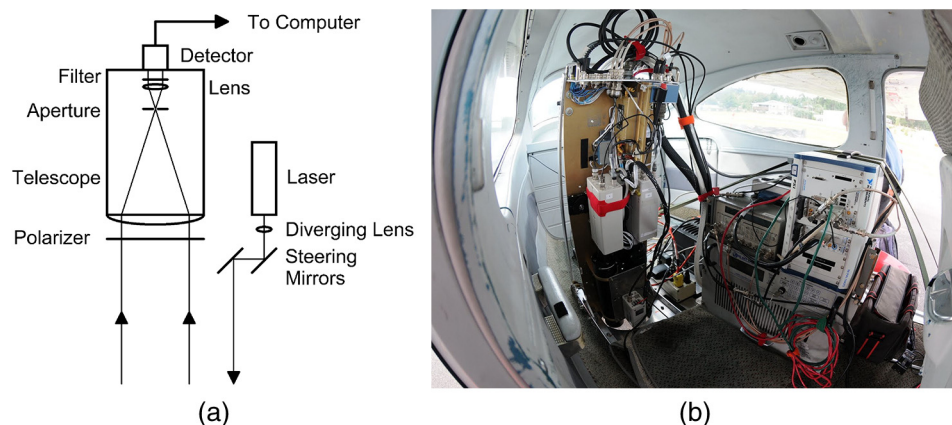


Fig. 2 Lidar system. (a) Schematic diagram of the laser transmitter optics and the receiver optics for one of the two receiver channels; (b) wide-angle photo of the lidar looking toward the rear of the aircraft. On the left is the receiver side of the optics package with the two telescopes at the bottom and the photomultiplier tube modules near the center. The laser and transmitter optics are out of view on the far side of the mounting plate. On the right, behind the pilot's seat, is the stack of electronics, including the laser cooling system (bottom), laser power supply, time-delay generator (top left), and data-acquisition package (top right).

of the peak return was identified for each lidar shot, and the positions of the maximum depths of the internal-wave oscillations were found. Because of the large number seen on September 16, the analysis concentrated on that day.

In situ instrumentation comprised a Seabird conductivity, temperature, depth (CTD) profiler with a Wetlabs AC-9 to measure the optical absorption and beam attenuation coefficients. Conductivity was used to calculate salinity, which was combined with temperature to provide density as a function of depth. The scattering coefficient was estimated as the difference between the attenuation and absorption coefficients.

Photographs of the surface manifestations of the internal waves were taken through the aircraft window with a Nikon D300 digital camera using an 18- to 200-mm focal length zoom lens. The combination of a periodic displacement of a subsurface scattering layer with a corresponding surface slick at the surface provides strong evidence for internal waves; other mechanisms could produce perturbations of the scattering layer or surface slicks, but it would be highly unlikely that these would occur together. The orientation and length of the surface slicks in the photographs also provide information on the direction of propagation and the width of the wave packet that are difficult to infer from the lidar alone.

To infer the width of the internal wave packet from one of the photographs (not presented), we had to correct for the geometric distortion caused by the oblique view angle. The field of view is easily obtained from the focal length of the zoom lens, which was recorded for each image. This leads directly to the angle with respect to the optical axis represented by each pixel in the image. We assumed that the camera was pointed at some angle α_0 below the horizon with the horizontal axis of the image parallel to the horizon. The position of each pixel on the surface can then be written as

$$x_{ij} = H \cot(\alpha y_{ij} - \alpha_0) \sin(\alpha x_{ij}) \quad y_{ij} = H \cot(\alpha y_{ij} - \alpha_0) \cos(\alpha x_{ij}), \quad (1)$$

where x_{ij} and y_{ij} are the position coordinates of the ij 'th pixel on the surface perpendicular to and along the optical axis, respectively, H is the aircraft altitude, αx_{ij} and αy_{ij} are the angles (in the x and y axes) of the ij 'th pixel. To estimate the angle α_0 , we selected two pixels at opposite sides of the mouth of White Beach Bay and calculated the distance between them in the corrected image, varying α_0 until the calculated distance agreed with the actual distance of 1520 m obtained from the nautical chart.

We also looked for evidence of stratified turbulence in plankton layers by calculating the power spectrum of fluctuations in the lidar return along center of the layer. This investigation used data from a previous deployment to East Sound, because those data could be compared with *in situ* samples of zooplankton. Biological sampling was not done in 2011.

3 Internal Waves

Figure 3 is an example of the processed lidar data for one of the internal waves. The background layer depth here was about 4 m, and the maximum depth of the internal wave was 7.8 m. This large perturbation, almost equal to the layer depth, suggests nonlinear propagation. Furthermore, two additional traits provide supporting evidence for this hypothesis. The first is the nonsymmetric shape of the wave, which is sharper on the trough and more rounded on the crest. The second is the fact that these waves were visible from the aircraft, because of the modulation of surface roughness by the currents induced by the waves.

In all, 10 observations of internal waves were clearly seen in the lidar data of September 16, two in the morning and eight in the afternoon. The positions of the troughs (maximum depths) of the afternoon observations are shown in Fig. 4, along with the afternoon flight tracks. All of the waves identified were near the mouth of White Beach Bay.

The *in situ* profile measured at the northern of the two locations (Fig. 5) shows a scattering layer at a depth of 3.4 m, which is just below the depth where the density gradient is greatest. The density profile has several step-like features, which are often related to different episodes of wind mixing followed by re-stratification. It is useful to consider a two-layer approximation as a simple model of the complex structure in the density profile. This was done by simply picking density values that seemed representative of the shallowest and deepest waters. The transition

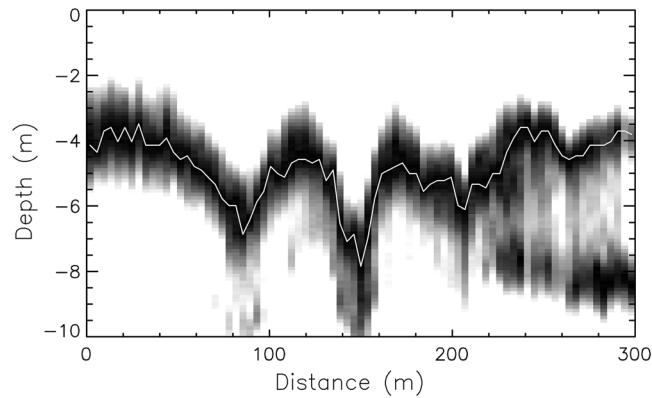


Fig. 3 Example of the relative lidar return across an internal wave (white to black represents 0 to 1) as a function of distance along the flight track and depth. Each lidar profile has been normalized by its maximum value, and the depth of that maximum is plotted as a white line.

was set at the depth where the actual density was equal to the midpoint between the shallow- and deep-water values.

For a two-layer ocean, the speed of propagation of a small (i.e., linear) internal wave is given by:

$$c_{\text{lin}} = \left[g \left(1 - \frac{\rho_1}{\rho_2} \right) \frac{h_1 h_2}{h_1 + h_2} \right]^{\frac{1}{2}}, \quad (2)$$

where g is the gravitational acceleration (9.8 m s^{-2}), ρ_1 is the density of the upper layer (1021.7 kg m^{-3}), ρ_2 is the density of the lower layer ($1022.53 \text{ kg m}^{-3}$), h_1 is the thickness of the upper layer (2.57 m), and h_2 is the thickness of the lower layer (16.53 m). Total water depth here ($h_1 + h_2$) was 19.1 m. The two-layer model for this case predicts a propagation speed of 13 cm s^{-1} . For weakly nonlinear internal waves, the Korteweg–de Vries (KdV) equation predicts a propagation speed of:³⁵

$$c_{\text{KdV}} = c_{\text{lin}} \left[1 - 0.5 \left(\frac{h_2 - h_1}{h_1 h_2} \right) A \right], \quad (3)$$

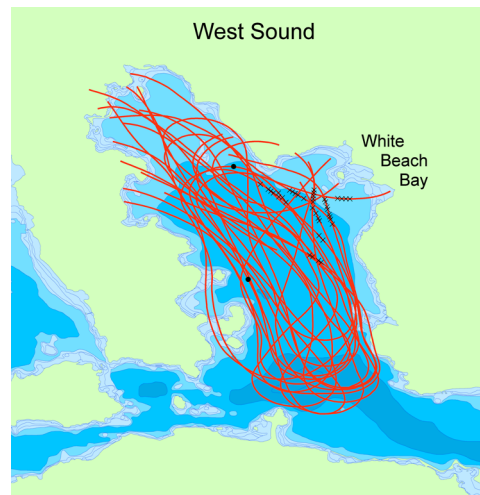


Fig. 4 West Sound with flight tracks (red or gray lines), crests of internal waves (black x), and locations of *in situ* measurements (black circles) from observations on the afternoon of September 16.

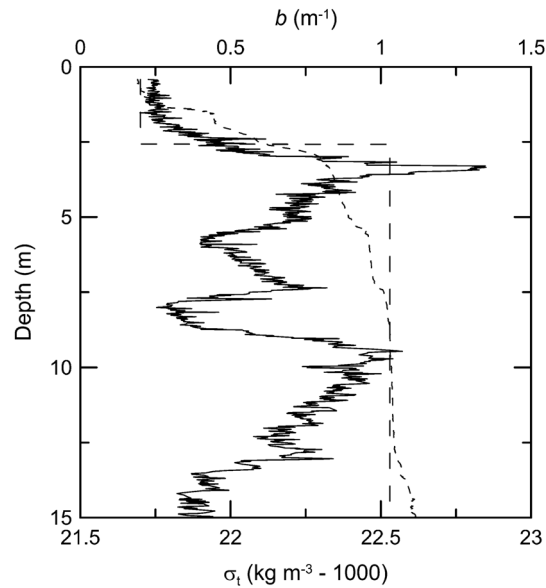


Fig. 5 Profiles of density, σ_t (short-dashed line), a rough two-layer approximation to σ_t (long-dashed line), and optical scattering coefficient b (black line) at a wavelength of 532 nm. The measurement location was the northernmost of the two *in situ* measurements marked in Fig. 4. The total water depth at this location was 19.1 m.

where A is the wave amplitude. For example, nonlinear effects would reduce the speed to 11 cm s^{-1} in a wave with a 1 m amplitude.

Consider the internal wave of Fig. 3. The water depth is about the same (19.1 m), but the thickness of the upper layer is 4 m, and the wave amplitude is 3.8 m. The layer densities are likely to be similar to the measured profile, so the KdV equation would predict a propagation speed of 5 cm s^{-1} . We made a second pass over the same area along the same direction 31 min later. The wave had clearly evolved in that time, but we could line up the main peaks by shifting the second record south by 87 m. Dividing 87 m by 31 min, we obtain a wave speed of 4.7 cm s^{-1} , which is in good agreement with the KdV prediction. This is more evidence for the nonlinear nature of the wave, since the linear approximation predicts a speed of 16 cm s^{-1} .

Numerical simulations,³⁶ field measurements,³⁷ and remote sensing observations³⁸ have all shown that the polarity of a nonlinear internal wave in a two-layer ocean depends on the relative thickness of the two layers. If the upper layer is thinner, as in the case of Fig. 3, the wave will manifest as a downward perturbation of the original layer. This polarity is clear from the figure. If the bottom layer is thinner, the perturbation will be upward. Figure 6 depicts one such example,

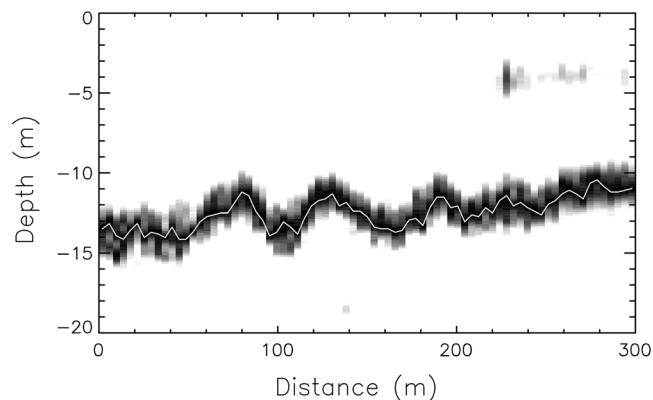


Fig. 6 Example of the relative lidar return across an internal wave (white to black represents 0 to 1) as a function of distance along the flight track and depth. Each lidar profile has been normalized by its maximum value, and the depth of that maximum is plotted as a white line.

where the top layer is thicker than the bottom layer; in this case, the scattering layer is deeper than the example in Fig. 3 and is perturbed upward by the internal wave.

The energy within an internal-wave field can be inferred from the aerial observations as well. We note that the potential energy of a small volume of water dV is given by

$$dE_p = \rho g z dV, \quad (4)$$

where z is depth. In the two-layer approximation, integrating both sides yields

$$E_p = 0.5(\rho_2 - \rho_1)Wg \int dx[h^2(x) - h_1^2], \quad (5)$$

where W is the width of the internal-wave field, h is the actual depth of the upper layer under the influence of the internal wave, and x is in the direction of propagation. The total energy is the sum of potential and kinetic energy, which are nearly equal.³⁹ Therefore $E = 2E_p$. Two passes of the lidar provide the amplitude and phase speed from which the density difference can be inferred. The integral is provided directly from the lidar. The width can be inferred from observations of the surface perturbation or from repeated passes of the lidar. For the case of Fig. 3, we estimated the width to be 420 m using the distance between pixels at opposite ends of one of the slicks in a photograph of the surface manifestation after applying the correction for geometric distortion described in Sec. 2. We estimated the other parameters from the lidar data to get a total energy of 9 MJ. The area of this wave train on the surface is about 420 by 200 m, so the average energy density is about 100 J m^{-2} . At the measured velocity of 4.7 cm s^{-1} , the 200-m-long wave train will pass a point in 4300 s, so the power moving up West Sound is 2.1 kW.

4 Turbulence

In a strongly stratified body of water, the energy contained within the internal waves is converted to turbulent energy at large scales through nonlinear interactions, and this energy cascades through smaller scales. The resulting spectra of potential and kinetic energy are predicted to be⁴⁰

$$E_p = 0.51 \varepsilon_p \varepsilon_K^{-1/3} k^{-5/3} \quad E_K = 0.51 \varepsilon_K^{2/3} k^{-5/3}, \quad (6)$$

where ε is the dissipation of potential or kinetic energy and k is the horizontal wavenumber. The $5/3$ power law was originally derived for homogeneous and isotropic turbulence, but appears also to be valid for the horizontal spectra of a thin layer of turbulence at spatial scales much greater than the layer thickness.⁴¹

To the extent that plankton drift with the local fluid motion, we can consider them to be passive additives that would have a horizontal spatial spectrum similar to that of the turbulent energy. That implies that β , the volume scattering function at the lidar wavelength and scattering angle (π rad), would also have a similar power spectrum⁴²

$$E_\beta = 0.51 \varepsilon_\beta \varepsilon_K^{-1/3} k^{-5/3}, \quad (7)$$

where ε_β represents the dissipation rate of the variance of β fluctuations. This is directly related to the dissipation of the variance of plankton number density, but the relationship depends on the volume scattering function of the individual organisms. There is very little information on these relationships, especially for cross-polarized scattering from nonspherical organisms.^{43,44}

Previous lidar measurements⁴⁵ of the horizontal spatial power spectrum of lidar backscatter produced a $-3/2$ dependence rather than the $-5/3$ dependence predicted by stratified-turbulence theory. Horizontal power spectra in East Sound and West Sound also failed to produce a $-5/3$ power law. In the theory, the turbulent layer is at a constant depth where the background density is assumed to be constant. In the real ocean, the layer is expected to follow the constant-density surface, which is not at a constant depth. If, instead of the return from a fixed depth, we select the return from the center of the layer and calculate the power spectrum of this quantity, we can sometimes see the predicted $-5/3$ dependence over the extent of a layer (Fig. 7).

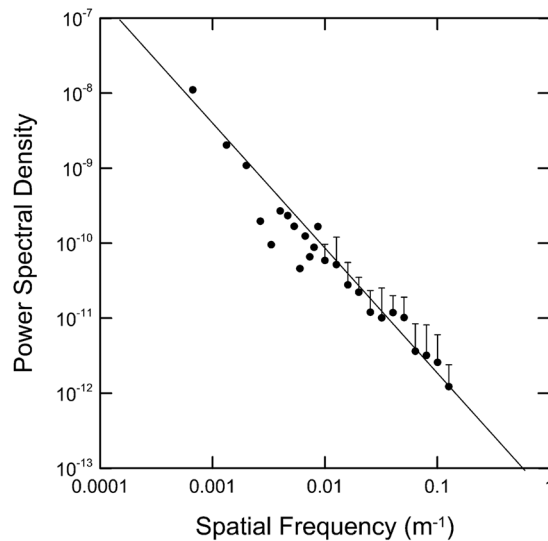


Fig. 7 Example of measured power spectral density of lidar return along a layer as a function of spatial frequency. For clarity of presentation, spectral values have been averaged for wavelengths less than 100 m and the positive error bar represents one standard deviation of the initial values. The line is a $-5/3$ power law.

Some layers failed to produce a clear power-law spectrum, however. The data presented in Fig. 7 were taken during a previous deployment to East Sound where extensive *in situ* sampling confirmed that almost no zooplankton were present within the layer. Other layers in the previous measurements contained significant numbers of zooplankton, and no clear power law spectrum was observed. Generally, zooplankton are more mobile than phytoplankton and are less likely to be true passive additives. In addition, some phytoplankton (e.g., dinoflagellates) have limited mobility, which has been shown to affect ocean color patterns⁴⁶ and may be enough to violate the passive-additive assumption. In other instances, the reason was not as clear, but lidar data may be useful in deciding whether or not the dominant mixing process within a layer is stratified turbulence.

5 Polarization Effects on Contrast

The layers that allowed detection of the internal waves were easier to see in the cross-polarized return than the co-polarized return. This effect can be evaluated quantitatively by considering layer contrast under different polarization conditions. For each shot, we define the contrast of the depolarized signal in terms of S , the cross-polarized lidar signal after correction for attenuation, as

$$C_x = \frac{S_{x_{\max}} - S_{x_{\min}}}{S_{x_{\max}} + S_{x_{\min}}}, \quad (8)$$

where $S_{x_{\max}}$ and $S_{x_{\min}}$ are the maximum and minimum values of the signal within the depth range, respectively. For this analysis, we used a depth range of 2 to 10 m. The top 2 m are contaminated by surface reflections and bubbles in high winds, and the signals are noisy below 10 m in some areas.

To ensure that we were focusing the analysis on the scattering layers, the data were separated into 10 s segments, and the shot with the highest contrast within each segment was selected for further analysis. This time period corresponds with a horizontal distance of about 400 m, and visual inspection of the data suggests that this is sufficient to include a strong layer in most cases. For the selected data, we calculated the contrast of the co-polarized signal at the same depths as C_x and the depolarization as the ratio of $S_{x_{\max}}$ to the co-polarized signal at the same depth.

The contrast, plotted in Fig. 8, shows variability from flight to flight, but the depolarized contrast is clearly higher. For the linear polarization, average contrast was 0.13 ± 0.03 for the co-polarized signal and 0.25 ± 0.04 for the cross-polarized case. This difference is statistically significant ($p < 0.001$ in a two-sided t -test). For the circularly polarized cases,

the corresponding values are 0.18 ± 0.04 and 0.26 ± 0.01 , which also represents a statistically significant difference ($p = 0.010$). Interestingly, the contrast values for the linear and circular cross-polarized signals were not significantly different ($p = 0.77$). For the co-polarized signals, the difference between linear and circular polarization was larger ($p = 0.046$), but still only bordering on significant even if a low standard of $p < 0.05$ is adopted.

The lack of a significant difference in contrast between linear polarization and circular polarization suggests that both linear and circular depolarization carry the same information. In 1957, van de Hulst²⁴ used symmetry arguments to show that the Mueller matrix for the case of interest for lidar (scattering angle of 180 deg) from a collection of particles was diagonal with only three parameters as long as each particle is accompanied by its mirror image. Hu et al.²⁵ showed that two of these parameters were related for backscattering for even a single dielectric particle. Mishchenko and Hovenier²⁶ combined these two results to obtain the following Mueller scattering matrix:

$$\mathbf{M} = \beta(\pi) \begin{bmatrix} 1 & 0 & 0 & 0 \\ 0 & 1-d & 0 & 0 \\ 0 & 0 & d-1 & 0 \\ 0 & 0 & 0 & 2d-1 \end{bmatrix}, \tag{9}$$

where $\beta(\pi)$ is the volume backscatter coefficient at 180 deg and d is the single polarization parameter.

This implies that the depolarization of an initially polarized beam will be

$$D_L = \frac{d}{2-d} \quad D_C = \frac{d}{1-d} \tag{10}$$

where D is the ratio of the backscattering perpendicular to the incident polarization to that in the same polarization for incident light that is either linearly (L) or circularly (C) polarized. If this Mueller matrix applies, we should be able to predict what the circular depolarization should be based on the linear depolarization according to the following relationship:

$$D_C = \frac{2D_L}{1-D_L}. \tag{11}$$

Average depolarization values (Fig. 9) suggest that the circular depolarization is greater than linear, as predicted. Overall, we have $D_L = 0.06 \pm 0.01$ and $D_C = 0.11 \pm 0.03$, and the difference is statistically significant ($p = 0.028$). For the cases with linear polarization, we have also

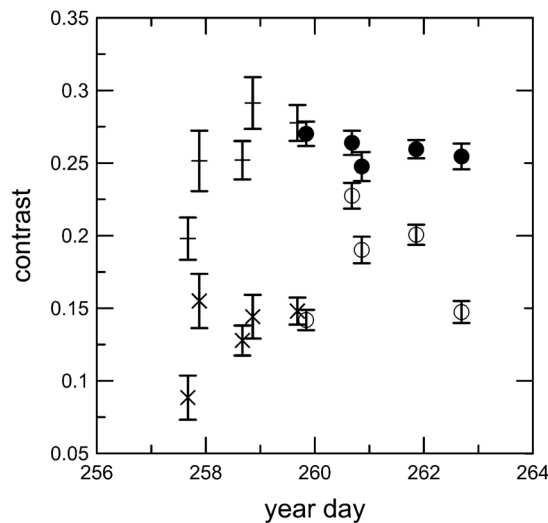


Fig. 8 Optical contrast by flight as a function of year day, 2011. Symbols denote linear cross-polarized (+), linear co-polarized (x), circular cross-polarized (*) and circular co-polarized (o) values. Error bars denote \pm one standard deviation of the values measured during each flight.

estimated what the circular polarization would have been if Eq. (10) is valid. The overall average is 0.13 ± 0.02 , which is not statistically different ($p = 0.28$) from the actual measurements using circular polarization. This is consistent with recent measurements of atmospheric scattering.^{47–50}

6 Surface Manifestations

As noted in the introduction, internal waves can be detected by microwave radar because the induced surface currents modulate the surface roughness. This same process affects the amount of skylight reflected from the surface. The reason is that the Fresnel reflectivity from the surface is not a linear function of incident angle, so the average reflectivity of a roughened surface at some nominal view angle is not the same as the reflectivity of a flat surface at the same angle. The magnitude of the effect depends on the view angle, surface roughness, and polarization of the skylight, but can be a few percent for view angles of 60 deg to 70 deg from nadir and root-mean-square surface angles near 5 deg.

A photograph taken from the aircraft (Fig. 10) shows the surface signature of one of the wave packets observed. While the information is in the original image, it is much more visible after contrast enhancement. The black line added to the original image crosses three slicks associated with the wave. Figure 11 is a plot of relative pixel value in the green channel of the original color image from the bottom of this line to its top. A linear regression of pixel value was used as the background value, since there was a nearly linear change in illumination along the line. The relative value at each pixel is then estimated as the difference between the pixel value and the regression value, normalized by the regression value. The three slicks are clearly visible, with peak values of about 2%, as expected from the Fresnel reflectivity estimates.

The presence of the surface manifestation is important for interpreting the lidar data, because it provides the direction of the wave fronts. With this information, we were able to calculate internal wave wavelength and phase speed in Sec. 3, knowing that our flight track crossed the waves nearly normal to the wave front. Without this information, the angle between the phase front and the lidar track is uncertain, and the estimate of wavelength is subject to error. We should point out that the wavelength could also be inferred from the image in Fig. 10, but to do this quantitatively would require a correction of the geometric distortion of the image as described in Sec. 2. This was not done for this image, because we obtained the wavelength from the lidar data.

Remotely sensing the surface manifestation alone misses important information. There have been attempts to infer the depth of the pycnocline from the surface manifestations of internal waves, but with limited success.^{51,52} These have only been made for a two-layer model of ocean

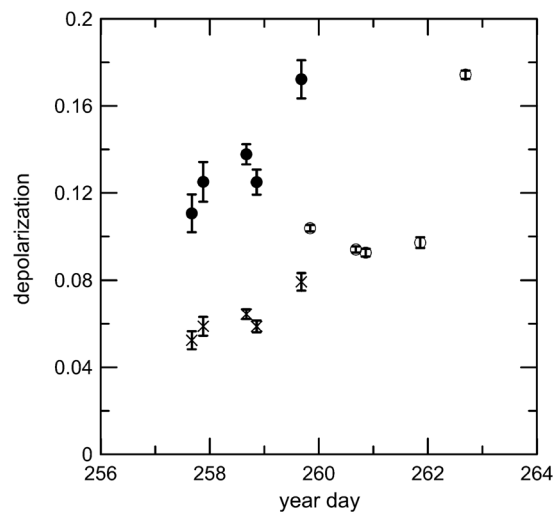


Fig. 9 Layer depolarization by flight as a function of year day, 2011. (x) is linear depolarization, (o) is circular depolarization, and (•) is circular depolarization predicted from the measured linear depolarization. Error bars denote \pm one standard deviation of the average of each flight.



Fig. 10 Photo of the surface signature of one of the observed internal waves: (a) original with a black line marking the section plotted in Fig. 11; (b) same image after contrast enhancement.

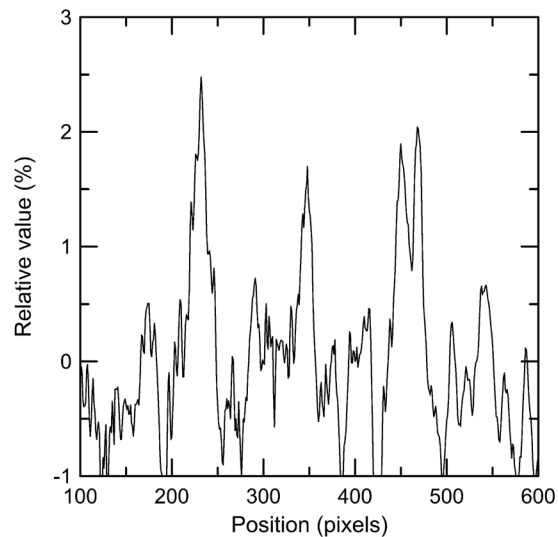


Fig. 11 Relative pixel value above background level as a function of position along the black line in Fig. 10(a) (bottom to top).

density profile and require multiple observations. The amplitude of the wave is not possible to measure. The primary advantage of radar detection of the surface manifestation is that it is possible from space; there are currently no orbiting lidar systems capable of internal-wave detection. The closest is the NASA Cloud-Aerosol Lidar with Orthogonal Polarisation (CALIOP), but it lacks both the vertical and horizontal resolution for this application.⁵³

7 Conclusions

Airborne lidar can easily detect nonlinear internal waves in a shallow fjord when conditions are right to produce a plankton layer associated with a density gradient. The propagation of these waves seems to be fairly well modeled by a two-layer ocean model and the KdV equation. While there were almost certainly linear internal waves in West Sound during our measurement period, their amplitudes would have had to have been much less than 1 m for nonlinear effects to be negligible. Detection of these would require more sophisticated processing to discriminate between internal waves and random variability.

The observed $-5/3$ power law spectrum of lidar backscatter along the layer suggests that stratified turbulence played an important role in producing the variability in lidar backscatter. This spectral dependence is a necessary, but not sufficient condition for stratified turbulence, and more work is needed to establish the reliability with which turbulent mixing within a layer can be identified.

The layers that create the lidar signal can most easily be observed using a polarized transmitter and a cross-polarized receiver, but there is no significant difference in contrast between lidars using linear or circular polarization. The reason for this seems to be that the single-parameter Mueller matrix that has been used for atmospheric lidar studies is also valid for scattering from plankton layers in the ocean.

When surface manifestations of internal waves are visible, these can provide additional information about the direction of propagation and width of the wave front. This can be done reliably with visible images, even if the contrast is low. The combination of lidar and surface imagery provides the total energy in an internal-wave packet.

Acknowledgments

This work was partially supported by the Office of Naval Research under Grants N0001410IP20035 and N000140811217. Our pilot was Jay Palmer.

References

1. C. Garrett, "Internal tides and ocean mixing," *Science* **301**(5641), 1858–1859 (2003), <http://dx.doi.org/10.1126/science.1090002>.
2. M. H. Alford, "Redistribution of energy available for ocean mixing by long-range propagation of internal waves," *Nature* **423**(6936), 159–162 (2003), <http://dx.doi.org/10.1038/nature01628>.
3. T. H. Bell, Jr., "Topographically generated internal waves in the open ocean," *J. Geophys. Res.* **80**(3), 320–327 (1975), <http://dx.doi.org/10.1029/JC080i003p00320>.
4. C. R. Jackson, J. C. B. da Silva, and G. Jeans, "The generation of nonlinear internal waves," *Oceanography* **25**(2), 108–123 (2012), <http://dx.doi.org/10.5670/oceanog>.
5. H. van Haren and L. Gostiaux, "Energy release through internal wave breaking," *Oceanography* **25**(2), 124–131 (2012), <http://dx.doi.org/10.5670/oceanog>.
6. J. R. Apel and F. I. Gonzalez, "Nonlinear features of internal waves off Baja California as observed from the SEASAT imaging radar," *J. Geophys. Res.* **88**(C7), 4459–4466 (1983), <http://dx.doi.org/10.1029/JC088iC07p04459>.
7. L.-L. Fu and B. Holt, "Internal waves in the Gulf of California: observations from a spaceborne radar," *J. Geophys. Res.* **89**(C2), 2053–2060 (1984), <http://dx.doi.org/10.1029/JC089iC02p02053>.
8. R. A. Kropfli et al., "Relationships between strong internal waves in the coastal zone and their radar and radiometric signatures," *J. Geophys. Res.* **104**(C2), 3133–3148 (1999), <http://dx.doi.org/10.1029/98JC02549>.
9. J. F. Vesecky and R. H. Stewart, "The observation of ocean surface phenomena using imagery from the SEASAT synthetic aperture radar: an assessment," *J. Geophys. Res.* **87**(C5), 3397–3430 (1982), <http://dx.doi.org/10.1029/JC087iC05p03397>.
10. D. R. Lyzenga and J. R. Bennett, "Full-spectrum modeling of synthetic aperture radar internal wave signatures," *J. Geophys. Res.* **93**(C10), 12345–12354 (1988), <http://dx.doi.org/10.1029/JC093iC10p12345>.
11. D. R. Thompson, "Calculation of radar backscatter modulations from internal waves," *J. Geophys. Res.* **93**(C10), 12371–12380 (1988), <http://dx.doi.org/10.1029/JC093iC10p12371>.
12. A. K. Hanson and P. L. Donaghay, "Micro- to fine-scale chemical gradients and layers in stratified coastal waters," *Oceanography* **11**(1), 10–17 (1998), <http://dx.doi.org/10.5670/oceanog>.
13. W. M. Durham and R. Stocker, "Thin phytoplankton layers: characteristics, mechanisms, and consequences," *Ann. Rev. Mar. Sci.* **4**(1), 177–207 (2011), <http://dx.doi.org/10.1146/annurev-marine-120710-100957>.
14. M. M. Deksheniaks et al., "Temporal and spatial occurrence of thin phytoplankton layers in relation to physical processes," *Mar. Ecol. Prog. Ser.* **223**, 61–71 (2001), <http://dx.doi.org/10.3354/meps223061>.
15. P. L. Donaghay and T. R. Osborn, "Toward a theory of biological-physical control of harmful algal bloom dynamics and impacts," *Limnol. Oceanogr.* **42**(5), 1283–1296 (1997), http://dx.doi.org/10.4319/lo.1997.42.5_part_2.1283.

16. F. E. Hoge et al., "Airborne Lidar detection of subsurface oceanic scattering layers," *Appl. Opt.* **27**(19), 3969–3977 (1988), <http://dx.doi.org/10.1364/AO.27.003969>.
17. A. P. Vasilkov et al., "Airborne polarized lidar detection of scattering layers in the ocean," *Appl. Opt.* **40**(24), 4353–4364 (2001), <http://dx.doi.org/10.1364/AO.40.004353>.
18. J. H. Churnside and P. L. Donaghay, "Thin scattering layers observed by airborne lidar," *ICES J. Mar. Sci.* **66**(4), 778–789 (2009), <http://dx.doi.org/10.1093/icesjms/fsp029>.
19. D. V. Holliday, C. F. Greenlaw, and P. L. Donaghay, "Acoustic scattering in the coastal ocean at Monterey Bay, CA, USA: Fine-scale vertical structures," *Continent. Shelf Res.* **30**(1), 81–103 (2010), <http://dx.doi.org/10.1016/j.csr.2009.08.019>.
20. J. H. Churnside and L. A. Ostrovsky, "Lidar observation of a strongly nonlinear internal wave train in the Gulf of Alaska," *Int. J. Remote Sens.* **26**(1), 167–177 (2005), <http://dx.doi.org/10.1080/01431160410001735076>.
21. G. D. Lewis, D. L. Jordan, and P. J. Roberts, "Backscattering target detection in a turbid medium by polarization discrimination," *Appl. Opt.* **38**(18), 3937–3944 (1999), <http://dx.doi.org/10.1364/AO.38.003937>.
22. X. Ni and R. R. Alfano, "Time-resolved backscattering of circularly and linearly polarized light in a turbid medium," *Opt. Lett.* **29**(23), 2773–2775 (2004), <http://dx.doi.org/10.1364/OL.29.002773>.
23. S. A. Kartazayeva, X. Ni, and R. R. Alfano, "Backscattering target detection in a turbid medium by use of circularly and linearly polarized light," *Opt. Lett.* **30**(10), 1168–1170 (2005), <http://dx.doi.org/10.1364/OL.30.001168>.
24. H. C. van de Hulst, *Light Scattering by Small Particles*, Dover, New York (1981).
25. C.-R. Hu, "Symmetry theorems on the forward and backward scattering Mueller matrices for light scattering from a nonspherical dielectric scatterer," *Appl. Opt.* **26**(19), 4159–4173 (1987), <http://dx.doi.org/10.1364/AO.26.004159>.
26. M. I. Mishchenko and J. W. Hovenier, "Depolarization of light backscattered by randomly oriented nonspherical particles," *Opt. Lett.* **20**(12), 1356–1358 (1995), <http://dx.doi.org/10.1364/OL.20.001356>.
27. G. G. Gimmetstad, "Reexamination of depolarization in lidar measurements," *Appl. Opt.* **47**(21), 3795–3802 (2008), <http://dx.doi.org/10.1364/AO.47.003795>.
28. J. E. B. Rines et al., "Thin layers and camouflage: hidden *Pseudo-nitzschia* spp. (Bacillariophyceae) populations in a fjord in the San Juan Islands, Washington, USA," *Mar. Ecol. Progr. Ser.* **225**, 123–137 (2002), <http://dx.doi.org/10.3354/meps225123>.
29. A. L. Alldredge et al., "Occurrence and mechanisms of formation of a dramatic thin layer of marine snow in a shallow Pacific fjord," *Mar. Ecol. Progr. Ser.* **233**, 1–12 (2002), <http://dx.doi.org/10.3354/meps233001>.
30. M. A. McManus et al., "Characteristics, distribution and persistence of thin layers over a 48 hour period," *Mar. Ecol. Progr. Ser.* **261**, 1–19 (2003), <http://dx.doi.org/10.3354/meps261001>.
31. J. H. Churnside and J. J. Wilson, "Airborne lidar for fisheries applications," *Opt. Eng.* **40**(3), 406–414 (2001), <http://dx.doi.org/10.1117/1.1348000>.
32. J. H. Churnside, "Polarization effects on oceanographic lidar," *Opt. Express* **16**(2), 1196–1207 (2008), <http://dx.doi.org/10.1364/OE.16.001196>.
33. J. H. Churnside, A. F. Sharov, and R. A. Richter, "Aerial surveys of fish in estuaries: a case study in Chesapeake Bay," *ICES J. Mar. Sci.* **68**(1), 239–244 (2011), <http://dx.doi.org/10.1093/icesjms/fsq138>.
34. H. M. Zorn, J. H. Churnside, and C. W. Oliver, "Laser safety thresholds for cetaceans and pinnipeds," *Mar. Mammal Sci.* **16**(1), 186–200 (2000), <http://dx.doi.org/10.1111/j.1748-7692.2000.tb00912.x>.
35. L. A. Ostrovsky and Y. A. Stepanyants, "Do internal solitons exist in the ocean?," *Rev. Geophys.* **27**(3), 293–310 (1989), <http://dx.doi.org/10.1029/RG027i003p00293>.
36. K. Saffarinia and T. W. Kao, "Numerical study of the breaking of an internal soliton and its interaction with a slope," *Dyn. Atmos. Oceans* **23**(1–4), 379–391 (1996), [http://dx.doi.org/10.1016/0377-0265\(95\)00428-9](http://dx.doi.org/10.1016/0377-0265(95)00428-9).
37. M. H. Orr and P. C. Mignerey, "Nonlinear internal waves in the South China Sea: Observation of the conversion of depression internal waves to elevation internal waves," *J. Geophys. Res.* **108**(C3), 3064 (2003), <http://dx.doi.org/10.1029/2001JC001163>.

38. Z. Zhao et al., "Estimating parameters of a two-layer stratified ocean from polarity conversion of internal solitary waves observed in satellite SAR images," *Remote Sens. Environ.* **92**(2), 276–287 (2004), <http://dx.doi.org/10.1016/j.rse.2004.05.014>.
39. J. N. Moum et al., "Energy transport by nonlinear internal waves," *J. Phys. Oceanogr.* **37**(7), 1968–1988 (2007), <http://dx.doi.org/10.1175/JPO3094.1>.
40. E. Lindborg, "The energy cascade in a strongly stratified fluid," *J. Fluid Mech.* **550**, 207–242 (2006), <http://dx.doi.org/10.1017/S0022112005008128>.
41. J. J. Riley and E. Lindborg, "Stratified turbulence: A possible interpretation of some geophysical turbulence measurements," *J. Atmos. Sci.* **65**(7), 2416–2424 (2008), <http://dx.doi.org/10.1175/2007JAS2455.1>.
42. G. Brethouwer and E. Lindborg, "Passive scalars in stratified turbulence," *Geophys. Res. Lett.* **35**(6), L06809 (2008), <http://dx.doi.org/10.1029/2007GL032906>.
43. O. Svensen et al., "Mueller matrix measurements of algae with different shape and size distributions," *Appl. Opt.* **50**(26), 5149–5157 (2011), <http://dx.doi.org/10.1364/AO.50.005149>.
44. R. D. Vaillancourt et al., "Light backscattering properties of marine phytoplankton: relationships to cell size, chemical composition and taxonomy," *J. Plankton Res.* **26**(2), 191–212 (2004), <http://dx.doi.org/10.1093/plankt/fbh012>.
45. J. H. Churnside and J. J. Wilson, "Power spectrum and fractal dimension of laser backscattering from the ocean," *JOSA* **23**(11), 2829–2833 (2006), <http://dx.doi.org/10.1364/JOSAA.23.002829>.
46. M. A. Montes-Hugo et al., "Ocean color patterns help to predict depth of Opt. layers in stratified coastal waters," *J. Appl. Remote Sens.* **5**(1), 053548–053548 (2011), <http://dx.doi.org/10.1117/1.3634055>.
47. X. Cao et al., "Comparison of the relationships between lidar integrated backscattered light and accumulated depolarization ratios for linear and circular polarization for water droplets, fog oil, and dust," *Appl. Opt.* **48**(21), 4130–4141 (2009), <http://dx.doi.org/10.1364/AO.48.004130>.
48. G. Roy, X. Cao, and R. Bernier, "On linear and circular depolarization lidar signatures in remote sensing of bioaerosols: experimental validation of the Mueller matrix for randomly oriented particles," *Opt. Eng.* **50**(12), 126001 (2011), <http://dx.doi.org/10.1117/1.3657505>.
49. M. Hayman and J. P. Thayer, "Explicit description of polarization coupling in lidar applications," *Opt. Lett.* **34**(5), 611–613 (2009), <http://dx.doi.org/10.1364/OL.34.000611>.
50. Y. Balin et al., "Application of circularly polarized laser radiation for sensing of crystal clouds," *Opt. Express* **17**(8), 6849–6859 (2009), <http://dx.doi.org/10.1364/OE.17.006849>.
51. J. H. Churnside and A. V. Smirnov, "Remote sensing of internal waves in the ocean," in *The Oceans: Physical-Chemical Dynamics and Human Impact* S. K. Majumdar, Ed., pp. 146–156, The Pennsylvania Academy of Science, Easton, Pennsylvania (1994).
52. X. Li, P. Clemente-Colon, and K. S. Friedman, "Estimating oceanic mixed-layer depth from internal wave evolution observed from Radarsat-1 SAR," *Johns Hopkins APL Technical Digest* **21**(1), 130–135 (2000).
53. D. M. Winker et al., "Overview of the CALIPSO Mission and CALIOP Data Processing Algorithms," *J. Atmos. Oceanic Technol.* **26**(11), 2310–2323 (2009), <http://dx.doi.org/10.1175/2009JTECHA1281.1>.



James H. Churnside received his PhD from the Oregon Graduate Center studying the statistics of optical propagation through refractive turbulence in the clear atmosphere. He then became a member of the Technical Staff of The Aerospace Corporation in Los Angeles working on atmospheric propagation and laser speckle statistics. Since 1985, he has been a physicist with the NOAA Earth System Research Laboratory and its predecessors. He is currently working on the development of airborne oceanographic lidar and applications to fisheries, marine ecosystems, and upper ocean dynamics. He has published 90 papers in peer-reviewed journals and holds four patents.



Richard D. Marchbanks is an associate scientist at the Cooperative Institute for Research in Environmental Sciences (CIRES) at the University of Colorado. His primary expertise is lidar and optical systems for remote sensing. Research includes development and application of ultraviolet differential absorption lidar (DIAL) systems, infrared wind lidar systems and ocean probing lidar systems. He earned his MS in electro-optical engineering from the University of New Mexico in 1995.



Jennifer H. Lee received her BS in 2003 from the California Institute of Technology and her PhD in 2011 from Cornell University in applied and engineering physics. She conducted her postdoctoral research in the Atmospheric Remote Sensing group at NOAA, where she investigated the correlation of airborne lidar returns and ground-based measurements of optical properties. She is currently a radiation effects engineer at Ball Aerospace and Technologies Corp.



Joseph A. Shaw is the director of the Optical Technology Center, professor of electrical and computer engineering, and affiliate professor of physics at Montana State University in Bozeman. He was previously with the National Oceanic and Atmospheric Administration (NOAA) Environmental Research Labs in Boulder, Colorado. He received his PhD and MS degrees in optical sciences from the University of Arizona, his MS degree in electrical engineering from the University of Utah, and his BS degree in electrical engineering from the University of Alaska. He conducts research on the development and application of radiometric, polarimetric, and laser-based optical remote sensing systems. He is a fellow of both the OSA and SPIE.

Alan Weidemann got his degree in 1985 in biology at the University of Rochester. He then went to Mississippi under a Naval Research Laboratory post-doc working on optical properties of the ocean. He has remained at Mississippi until the present working on measurements of optical properties with emerging instrumentation and the interpretation of active and passive remote sensing for coastal processes.



Percy L. Donaghay received his PhD in biological oceanography from Oregon State University. He is currently a senior research scientist at the University of Rhode Island. Much of his research over the last 20 years has focused on the dynamics and impacts of thin layers of bacteria, phytoplankton, and zooplankton. Thin layers are patches of plankton that range in thickness from 10 cm to 3 m, yet are sufficiently intense, persistent, and spatially continuous to affect critical biological and biogeochemical processes and/or the performance of optical, acoustical, and chemical sensors. This research has included the development of theoretical and numerical models of the underlying processes and their impacts; the development of instruments and 4-D sampling techniques to quantify controlling biological and physical structure and processes; a field program to test these models in the coastal ocean; and collaboration with small businesses to make the resulting technologies available to the broader community.